

ARTICLE

Open Access

# Assembling defined DNA nanostructures with anticancer drugs: a metformin/DNA complex nanoplatform with a synergistic antitumor effect for KRAS-mutated lung cancer therapy

Hang Qian<sup>1</sup>, Dong Wang<sup>1,2</sup>, Binfeng He<sup>1,3</sup>, Qian Liu<sup>1,4</sup>, Yu Xu<sup>1</sup>, Di Wu<sup>1</sup>, Chunfa Chen<sup>1</sup>, Wen Zhang<sup>1</sup>, David Tai Leong<sup>5</sup> and Guansong Wang<sup>1</sup>

## Abstract

Herein, a strategy is proposed to simultaneously deliver the small-molecule drug metformin and siRNA with self-assembled DNA nanostructures. The biomedical application of DNA nanostructures is highly promising but still in its infancy. DNA nanostructures as drug delivery vehicles are conventionally synthesized in a magnesium-containing buffer. We propose using an anticancer drug to assemble DNA nanostructures and deliver them with siRNA for synergistic anticancer therapy. The metformin cargo induces DNA self-assembly into well-defined, uniform nanostructures, producing a drug–DNA nanocomplex with multiple functionalities for cancer therapy. Both tile-based and DNA origami structures can be assembled with metformin. The as-prepared metformin/DNA nanocomplex showed high structural and thermal stability and enzymatic resistance in physiological settings. The metformin in the nanocomplex and the KRAS<sup>G12C</sup> siRNA exerted a strong, synergistic antitumor effect against KRAS-mutated non-small cell lung cancer (NSCLC) both in vitro and in vivo by suppressing the RAS/AKT/mTOR and AMPK/AKT/mTOR signaling pathways. The current study suggests that the assembly of complex DNA nanomaterials with carefully chosen small molecules is key to endowing DNA nanostructures with new functionalities and subsequently expanding their applications in multidisciplinary research fields.

## Introduction

Recently, the biomedical applications of programmable, self-assembled DNA nanostructures have received increasing attention. These nanostructures have been investigated as smart drug delivery vehicles<sup>1–6</sup>, sensors<sup>7–10</sup>, and bioimaging agents<sup>11,12</sup> and have shown great potential in multiple research fields<sup>13,14</sup>. Nevertheless, the negatively charged DNA backbone, high salt concentration during

synthesis, and vulnerability in body fluids greatly impede the application of DNA nanostructures for clinical use. More importantly, in addition to the powerful structural control exhibited by DNA nanostructures, the incorporation of new functionalities into DNA nanostructures is highly desirable to adapt them to potential applications. One way to incorporate new functionality into DNA nanostructures is to covalently modify the phosphorus backbones or sugar rings of DNA oligos with functional molecules. For example, floxuridine was integrated into DNA strands and then self-assembled into well-defined polyhedral structures with tunable size, morphology, and drug loading efficiency<sup>2</sup>. Similarly, the phosphorothioate DNA backbone was first decorated with paclitaxel and further assembled into paclitaxel-containing nanoparticles

Correspondence: David Tai Leong (cheltwd@nus.edu.sg) or Guansong Wang (wanggs@tmmu.edu.cn)

<sup>1</sup>Institute of Respiratory Diseases, Xinqiao Hospital, Third Military Medical University, Chongqing 400037, China

<sup>2</sup>Department of Respiratory Medicine, Jinling Hospital, Nanjing University, Nanjing, China

Full list of author information is available at the end of the article

These authors contributed equally: Hang Qian, Dong Wang, Binfeng He

© The Author(s) 2022



**Open Access** This article is licensed under a Creative Commons Attribution 4.0 International License, which permits use, sharing, adaptation, distribution and reproduction in any medium or format, as long as you give appropriate credit to the original author(s) and the source, provide a link to the Creative Commons license, and indicate if changes were made. The images or other third party material in this article are included in the article's Creative Commons license, unless indicated otherwise in a credit line to the material. If material is not included in the article's Creative Commons license and your intended use is not permitted by statutory regulation or exceeds the permitted use, you will need to obtain permission directly from the copyright holder. To view a copy of this license, visit <http://creativecommons.org/licenses/by/4.0/>.

with high drug loading ability<sup>3</sup>. Both of the obtained drug–DNA conjugated nanoparticles showed excellent antitumor effects and reversed drug resistance both *in vitro* and *in vivo*. In addition, antibodies were conjugated to DNA strands through two-step chemical reactions. The protein-labeled DNA strands further assembled into star-like DNA nanostructures with the proteins pointing out, mimicking pseudo-IgM<sup>15</sup>. Another promising strategy is to chemically or physically engineer the surface properties of DNA nanomaterials, such as by coating DNA nanostructures with a biocompatible layer or assembling DNA with functional guest molecules. Coating DNA nanostructures with a polymer layer significantly improved their stability in a low-salt environment and their resistance against DNase I by more than tenfold<sup>16</sup>. DNA nanostructures covered with proteins exhibited enhanced structural stability and immunocompatibility<sup>17</sup>. Endogenous polyamine-assembled origami DNA structures were shown to be stable in cell lysates and under high electrical voltage when subjected to electrotransfection<sup>18</sup>. In another study, spermidine was demonstrated to facilitate DNA assembly at constant temperatures, and a spermidine/DNA nanocomplex had higher cellular uptake efficiency in different cancer cells than Mg<sup>2+</sup>-assembled DNA nanostructures<sup>19</sup>. These findings suggest that engineering DNA nanostructure surface properties with cationic biomolecules is a promising way to endow DNA nanostructures with new functionalities and subsequently expand their applications.

Metformin and its analogs are well-known drugs that contain guanidino groups. Metformin contains two guanidino groups, was originally used as a common drug for diabetes, and has been intensively investigated as an anticancer drug in many cancer types. Chemically polymerized metformin with a spherical morphology exerted similar antitumor performances as metformin *in vivo*<sup>20</sup>. Guanidine is a monovalent cation under physiological conditions and a highly polar molecule in aqueous solution with an efficient resonance-stabilized positive charge. We thus anticipate that guanidino-containing molecules with high pKa values can induce DNA self-assembly into defined nanostructures under neutral or slightly acidic environments. We further envision that metformin not only “wraps” around the surface of DNA nanostructures as a protective layer but also serves as a functional moiety for potential cancer therapeutics.

Herein, we report a metformin/DNA complex nanoplateform consisting of the antitumor drug metformin and KRAS G12C mutation-specific (KRAS<sup>G12C</sup>) siRNA that exerts a significant synergistic effect to combat KRAS-mutated NSCLC. Both metformin and siRNA down-regulated mTOR and thus achieved a synergistic effect. G12C-specific siRNA was employed to avoid potential off-target effects. We first evaluated the metformin-induced

DNA self-assembly behaviors of both tile-based and origami DNA nanostructures in ultrapure water. Then, a metformin-assembled DNA nanotube carrying KRAS<sup>G12C</sup> siRNA was designed and synthesized as a model system. The anticancer effects of the metformin and KRAS<sup>G12C</sup> siRNA in the nanoplateform were thoroughly investigated both *in vitro* and *in vivo*. The underlying signaling pathways responsible for the synergistic effect of metformin and KRAS<sup>G12C</sup> siRNA were also validated. Our study demonstrates that metformin/DNA complex nanomaterials are excellent nanoplateforms that can serve as both drug and delivery vehicles and hold great potential in cancer therapeutics.

## Materials and methods

### DNA self-assembly

The component DNA strands for each structure were mixed together at the required molar ratio in metformin solution or Tris-Acetic-EDTA-Mg<sup>2+</sup> (TAE/Mg<sup>2+</sup>) buffer (pH 8.0) and then subjected to the following annealing process: 95 °C/5 min, 65 °C/30 min, 50 °C/30 min, 37 °C/30 min, and 22 °C/30 min. For KRAS<sup>G12C</sup> siRNA-loaded DNA nanotubes, the nanotubes with overhangs were first synthesized as mentioned above and then added to siRNA at a molar ratio of 1:6. The final mixtures were kept at room temperature for 30 min before use.

### PAGE

Six percent polyacrylamide (diluted from 40% 19:1 acrylamide/bis acrylamide) gel electrophoresis (PAGE) was run on a Bio-Rad Electrophoresis System (USA) at room temperature for 1 h at a constant voltage of 120 V. All DNA samples were mixed with 50% glycerol (at a DNA glycerol *v/v* ratio of 9:1) before loading into gel wells. The running buffer was TAE, and the gel was stained with Stains-all solution (0.01%).

### Agarose gel electrophoresis

One gram of agarose was dissolved in 50 mL of TBE buffer and then boiled *via* a microwave. GelRed (5 μL) was dropped into the cooled agarose solution before it was transferred into an electrophoresis chamber. Subsequently, a 2.0% agarose gel (w/v) was obtained after cooling to room temperature with a comb inserted. TBE buffer was used as a running buffer. The voltage used for electrophoresis was 80 V, and the running time was ~150 min. After electrophoresis, the gel was visualized under a Bio-Rad imaging system.

### AFM imaging

For AFM imaging, DNA nanotubes, tetrahedra, rectangles, and six-helix bundles were diluted to 50, 50, 10, and 10 nM, respectively. Five microliters of DNA sample solution was dropped onto a freshly cleaved mica surface

and incubated for 2 min to allow strong adsorption. The origami subject was purified by spin-columns with a molecular cutoff of 100 kDa (Pall, USA). The sample drop was then washed off using 50  $\mu\text{L}$  of 2 mM  $\text{Mg}(\text{Ac})_2$  solution and dried by compressed nitrogen. The DNA nanostructures were then imaged under ScanAsyst-air mode using a Multimode 8 AFM system (Bruker, USA) with silicon tips on a nitride lever (T: 650 nm, L: 115  $\mu\text{m}$ , W: 25  $\mu\text{m}$ ,  $f_0$ : 70 kHz, k: 0.4 N/m). The tip-surface interaction was automatically minimized.

#### DLS measurements

The concentrations of the tetrahedrons, nanotubes, rectangles, and six-helix bundle structures were 100, 100, 10, and 10 nM, respectively (Malvern Zetasizer, Malvern Instruments Laser Target Designator, UK). The solvents were either TAE/ $\text{Mg}^{2+}$  buffer or metformin solutions.

#### Cell culture

H358 and H23 cells were cultured in RPMI-1640 medium. The media all contained 10% fetal bovine serum (FBS), 100 units  $\text{mL}^{-1}$  penicillin, and 100  $\mu\text{g mL}^{-1}$  streptomycin. These cells were grown in a 95% humidified atmosphere of 5%  $\text{CO}_2$  at 37 °C. The cells were trypsinized and counted before each experiment when they grew to 80–90% confluence.

#### CLSM imaging

The internalization of DNA nanotubes was observed with a confocal laser scanning microscope (Leica, Germany). For confocal microscopy, cells were cultured in a 24-well plate with a coverslip over each well overnight at a density of  $1 \times 10^4$  cells/ $\text{cm}^2$  under standard culture conditions. Then, the cells were treated with Cy5-labeled DNA nanotubes for 12 h. DNA nanotubes were prepared with 300 mM metformin. The cells took up the Cy5 fluorophore, and the DNA nanotube concentrations were 300 and 50 nM. The volume ratio between the DNA sample and the medium was 1:9. After treatment, the cells were stained with Hoechst 33342 (final concentration: 1  $\mu\text{g mL}^{-1}$ ) for 30 min, washed with PBS 5 times and fixed with a mixture of 4% paraformaldehyde for 15 min. Finally, the cells were washed with PBS 3 times before imaging. Fluorescence images were obtained with an oil-immersion objective lens, excitation wavelengths of 405 and 543 nm, and emission wavelengths between 430/480 nm and 550/630 nm for Cy5 and Hoechst 33342, respectively.

#### Flow cytometry

For flow cytometry assays, cells were cultured in a 6-well plate overnight at a density of  $2 \times 10^4$  cells/ $\text{cm}^2$  and transfected with Cy5-labeled DNA nanotubes for 12 h. The cells took up the Cy5 fluorophore, and the DNA

nanotube concentrations were 300 and 50 nM. After being washed 3 times with PBS buffer, the cells were digested by trypsin and collected in PBS buffer with 2% FBS. The collected cells were centrifuged at 1500 rpm for 5 min and washed with PBS 2 times. Finally, the cells were resuspended in 350  $\mu\text{L}$  of PBS and subjected to flow cytometry (Backman, Gallios, USA).

#### Cell viability determination by MTT assay

Cells were cultured in a 96-well plate overnight with a seeding density of  $1 \times 10^3$  cells/well. Then, the cells were treated with different sample groups for 24 h. DNA nanotubes were prepared with 50 mM metformin in the presence of PEG. The cells were administered siRNA at a concentration of 300 nM. Finally, the viability was determined by the MTT assay.

#### RT-qPCR

Total RNA was isolated using TRIzol reagent according to the manufacturer's instructions and then reverse transcribed to cDNA. Quantitative real-time PCR was carried out using FastStart Universal SYBR Green Master Mix (Roche) on the BioRad CFX96 platform. The primer sequences for KRAS and  $\beta$ -actin were as follows: KRAS forward primer: 5'-AGTTGGAGCTGGTGGCGTAGG-3', KRAS reverse primer: 5'-TACTCCTCTTGACCTGCTGTGTCG-3';  $\beta$ -actin forward primer: 5'-GTGAAGGTGACAGCAGCAGTCGGTT-3',  $\beta$ -actin reverse primer: 5'-GAAGTGGGTGGCTTTAGGA-3'. The NT<sup>MgK</sup> concentration was 50 nM (siRNA and NC siRNA concentrations were 300 nM). The nanomaterials were incubated with cells for 24 h.

#### Western blotting

Western blotting was performed as previously described. Briefly, total proteins were extracted from the treated cells, and 40  $\mu\text{g}$  of each protein sample was separated by SDS-PAGE and transferred onto PVDF membranes. After blocking with nonfat milk, the membranes were incubated with primary antibodies overnight and then with the appropriate secondary antibody for 1 h. The protein signals were detected with an enhanced chemiluminescence ECL detection system. The densitometric analysis was performed using Quantity One software. Cells were administered siRNA and metformin concentrations of 300 and 30 mM, respectively. The nanomaterials were transfected for 6 h and then incubated with cells for another 24 h.

#### Evaluation of GTP-bound KRAS

The KRAS-GTP assay was carried out according to the manufacturer's instructions. using the Active Ras Detection Kit (CST, #8821S). Briefly, harvested cells were lysed with cell lysis buffer, and the lysate protein concentration

was determined using a BCA protein assay (Thermo Fisher). Then, at least 500  $\mu\text{g}$  of protein was incubated with GST-Raf1-RBD in a spin cup containing glutathione resin for 1 h at 4 °C. The GST-Raf1-RBD-protein complex was collected for further western blotting using a KRAS antibody.

#### Animal model

Six-week-old male mice were supplied by the Chinese Academy of Sciences (Shanghai, China). All animal experiments were conducted according to the laboratory animal care and use guidelines. All operations were approved by the Animal Ethics Committee of Xinqiao Hospital, Third Military Medical University. Briefly, 200  $\mu\text{L}$  of cell suspension containing  $2 \times 10^6$  cells was subcutaneously injected into the right flanks of Balb/c male nude mice.

#### In vivo antitumor assay

Tumor-bearing mice were randomly divided into five groups with six mice in each group. Different drug formulations were intravenously injected with equivalent doses of 1.66 mg of metformin (200  $\mu\text{L}$ , 50 mM) and 2.5 mg/kg KRAS<sup>G12C</sup> siRNA per mouse every other day for 3 times. Mice in the control group were treated with an equivalent volume of saline. The tumor width and length were recorded every 3 days during the treatment, and tumor volume was calculated according to the formula below: tumor volume =  $1/2 \times \text{width}^2 \times \text{length}$ . After the treatment, one mouse from each group was sacrificed, and the tissues were collected and excised for histological evaluation.

#### Histology and immunohistochemistry evaluations

For H&E staining, the excised tissues were fixed in 4% paraformaldehyde solution for at least 24 h, embedded in paraffin after dehydration, and sectioned into 5- $\mu\text{m}$ -thick slices. The tissue paraffin sections were deparaffinized through xylene and graded alcohol (100%, 85%, 75%) and washed with distilled water. Thereafter, tissue sections were stained with hematoxylin and eosin (H&E). The histological properties of tissues were observed and recorded under an optical microscope (CIC, XSP-C204).

The IHC assay was carried out according to our previous study. Tumor tissues were fixed and then subjected to immunohistochemical staining with the appropriate antibodies. Images were obtained with a Leica microscope (Leica Microsystems, Germany).

## Results

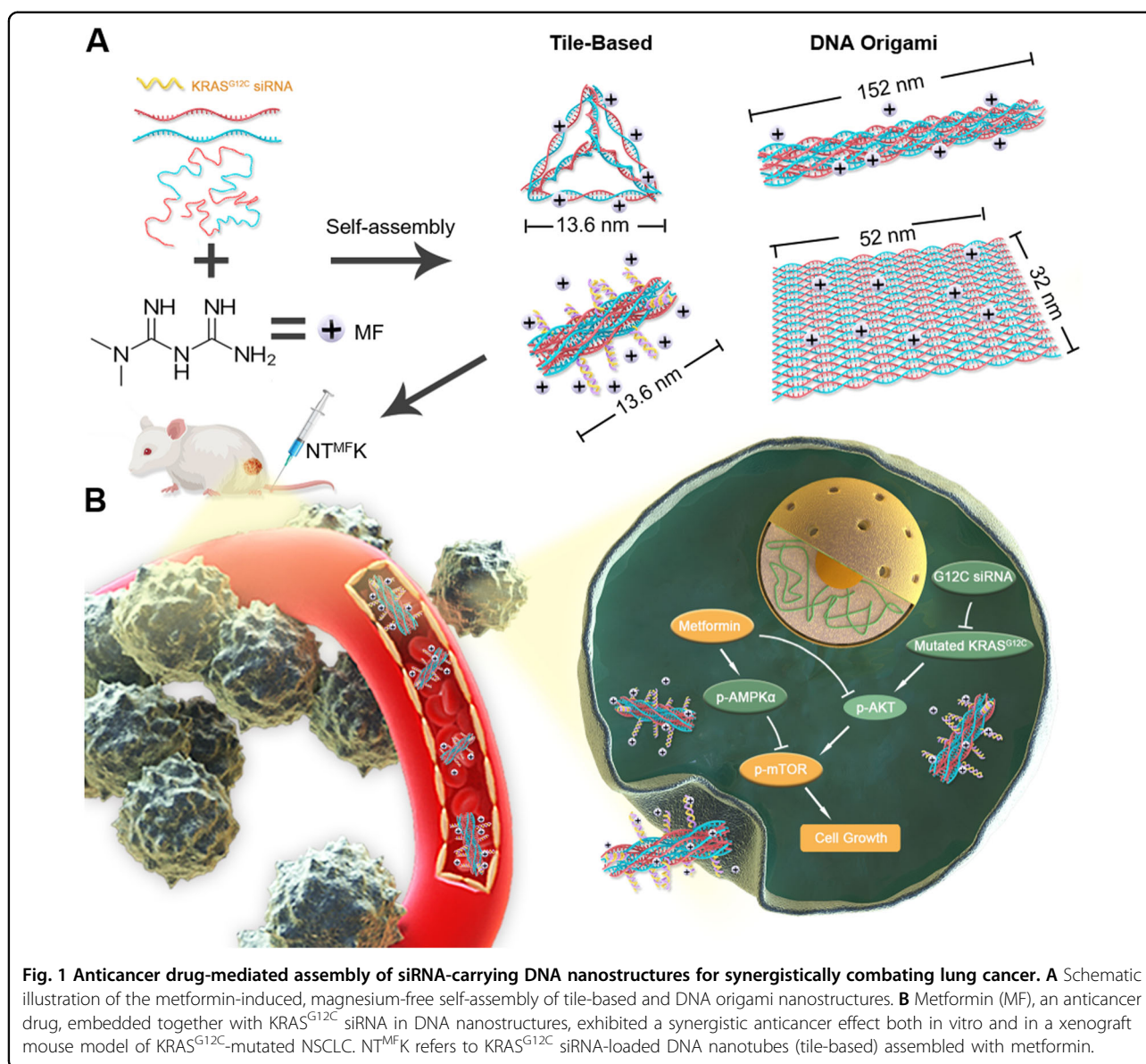
### Design of metformin-mediated DNA self-assembly for synergistic anticancer therapy

As shown in Fig. 1A, two tile-based DNA nanostructures (tetrahedrons and nanotubes) and two origami

DNA nanostructures (rectangles and six-helix bundles) were designed to validate the feasibility of magnesium-free, metformin-induced DNA nanostructure assembly. All DNA nanostructures were amenable to siRNA loading at an arbitrary ratio and with arbitrary positioning due to the remarkable structural control of the nanostructures. In our hypothesis, metformin induces DNA strand self-assembly into well-defined DNA nanostructures carrying a KRAS<sup>G12C</sup> siRNA payload through electrostatic interactions with DNA backbones. The strong binding between the positively charged guanidino groups and DNA makes metformin/DNA nanostructures a complex nanoplateform containing the anticancer drugs metformin and KRAS<sup>G12C</sup> siRNA. We further hypothesized that metformin and KRAS<sup>G12C</sup> siRNA would show a synergistic anticancer effect on KRAS<sup>G12C</sup>-mutated NSCLC (Fig. 1B).

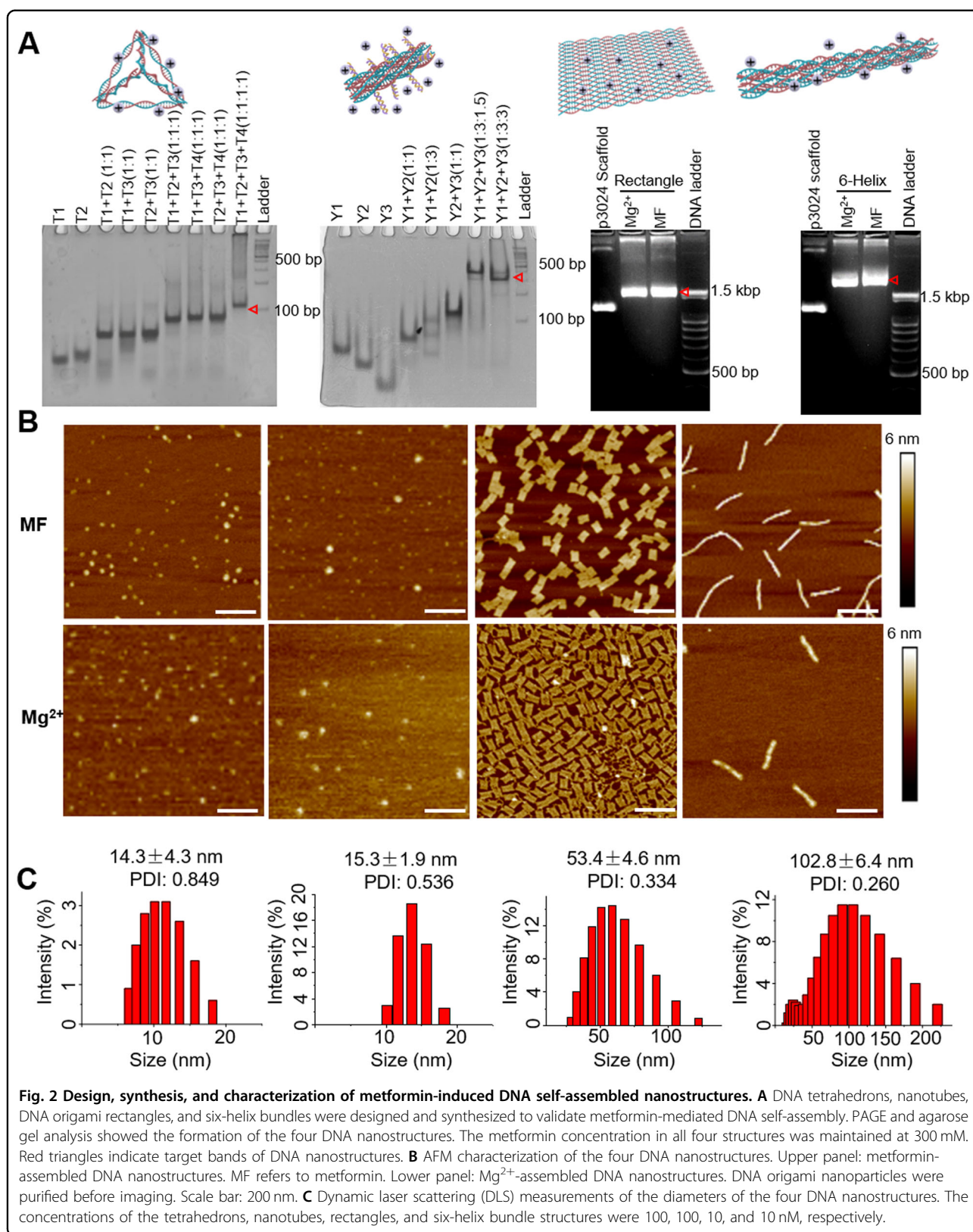
### Synthesis and characterization of metformin/DNA complex nanomaterials

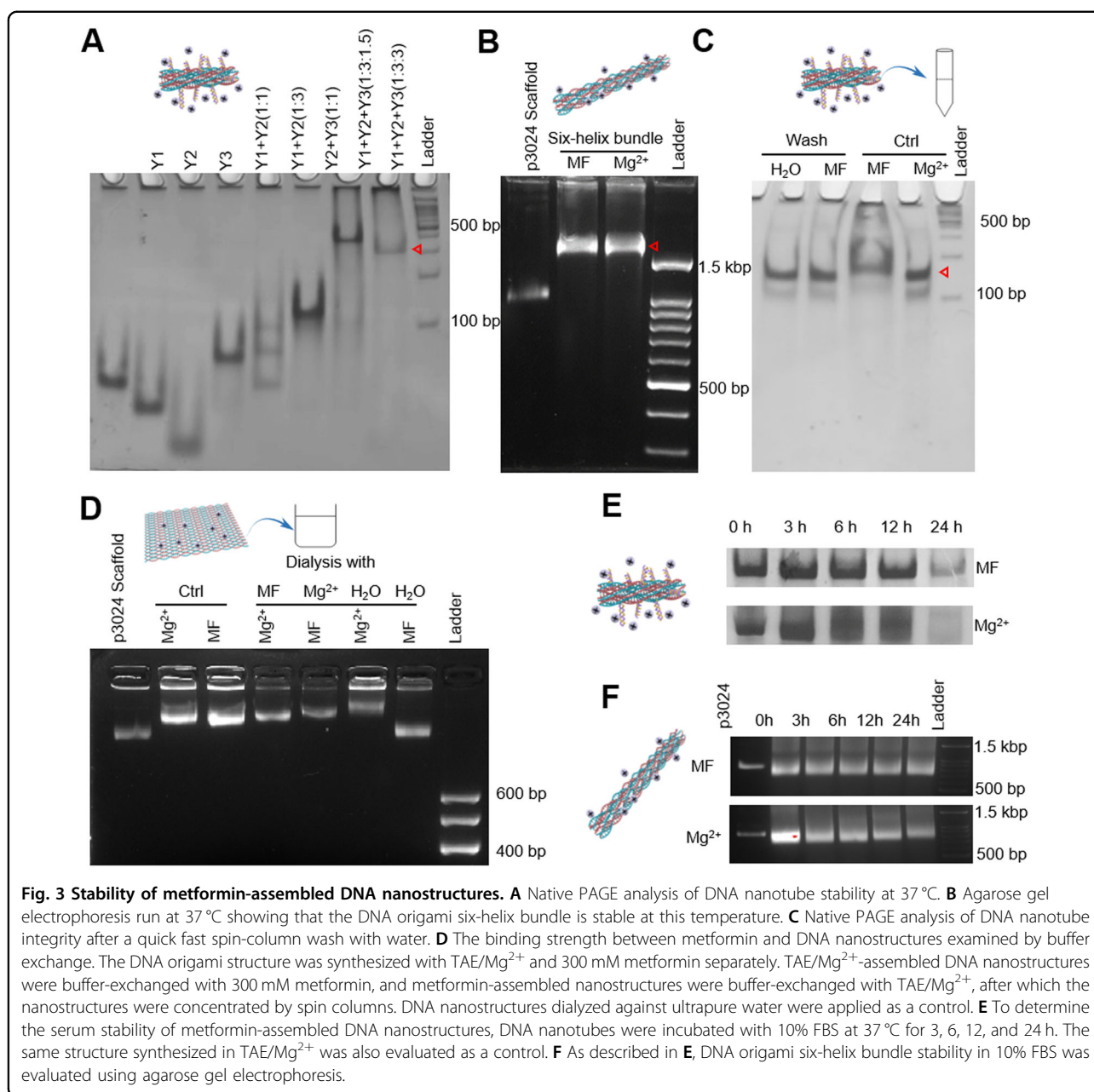
To explore metformin-induced DNA self-assembly behaviors, two tile-based DNA nanostructures were tested first. Four 55 nt DNA strands (Table S1), T1, T2, T3, and T4, hybridized with each other and folded into a tetrahedral structure<sup>17,21–23</sup>. Each edge of the tetrahedron was a single DNA duplex four turns long. The DNA nanotubes consisted of only three strands, Y1, Y2, and Y3 (Table S2), which were designed using a sequence symmetry strategy. One copy of Y1 and three copies of Y2 and Y3 were first assembled into a “Y”-shaped motif that then dimerized into a tubular structure by the 90-degree bending of each of its three arms<sup>24</sup>. To synthesize these structures, all component DNA strands for each structure were mixed with metformin in ultrapure water and then subjected to stepwise annealing. Polyacrylamide gel electrophoresis (PAGE) indicated that both DNA tetrahedrons and nanotubes migrated as dominant, sharp bands on the gel with reasonable mobilities compared with those of DNA ladders (Fig. 2A). Structures containing different combinations of individual strands showed intermediate product patterns on the gel identical to those of their Mg<sup>2+</sup>-assisted DNA counterpart samples (Fig. S1). For DNA origami, DNA scaffold p3024 and staple strands (for sequence information, see Tables S3–S5) were mixed and annealed to obtain the final structures (Schemes S1 and S2 in supporting information). Similarly, DNA origami rectangles and six-helix bundles formed well at metformin concentrations higher than 200 mM, as exhibited in the agarose gel in Fig. 2A (right two panels). The yields of DNA origami rectangles and six-helix bundles were 66.5% and 54.0%, respectively. In addition, the effect of metformin concentration on DNA nanostructure self-assembly was evaluated (Fig. S2). The minimum



metformin concentration required for successful self-assembly depended on the structural design. The minimum concentrations for the successful self-assembly of DNA tetrahedrons, nanotubes, rectangles, and six-helix bundles were estimated to be approximately 10, 300, 200, and 200 mM, respectively. Atomic force microscopy (AFM) imaging provided the strongest evidence of metformin-assembled DNA nanostructures (Fig. 2B, upper panel). Both DNA tetrahedrons and nanotubes (tile-based) were uniformly dispersed on mica surfaces. Height analysis implied that these structures were individual tetrahedrons and nanotubes (Fig. S3). As shown by the AFM images, the length and width of the DNA rectangles were approximately 78 and 55 nm, respectively, close to the values calculated based on its

theoretical design. The height of the DNA rectangles was  $\sim 2.1$  nm, indicating that metformin-assembled rectangles were present as a single-layer sheet on the mica surface (Fig. S4). The DNA origami six-helix bundles exhibited a length of  $\sim 178$  nm by AFM and a curved wire-shaped morphology (Fig. S5). The morphologies of  $Mg^{2+}$ -assembled DNA nanostructures were also imaged by AFM (Fig. 2B, lower panel). They showed similar characteristics for all four structures, and no profound differences were observed compared to metformin-assembled structure counterparts in the current experimental settings. Dynamic laser scattering (DLS) measurements indicated that the hydrodynamic diameters of the four structures were  $14.3 \pm 4.3$  nm,  $15.3 \pm 1.9$  nm,  $53.4 \pm 4.6$  nm, and  $102.8 \pm 6.4$  nm.





### Stability of metformin/DNA nanostructures

We first evaluated the thermal stability of metformin/DNA complexes at 37 °C. Agarose gel electrophoresis and PAGE run at 37 °C showed that both DNA nanotubes and the DNA six-helix bundles migrated as concentrated bands on the gel at reasonable molecular weights compared to the DNA ladder (Fig. 3A, B). This finding suggested that the binding of metformin to DNA is strong enough to maintain the DNA structure as a whole at 37 °C. To provide more convincing evidence of this strong binding, metformin/DNA nanocomplexes were subjected to spin-column washing and buffer exchange. Most of the

DNA nanotubes remained intact with a small amount of aggregation when subjected to a quick spin-column wash with water or 50 mM metformin (Fig. 3C). The majority of the metformin/DNA nanocomplexes (DNA rectangles are used as an example) remained intact after buffer exchange with TAE/Mg<sup>2+</sup> or water (Fig. 3D). These results indicated that the structural stability of metformin-assembled DNA nanostructures in the current study is sufficient for complicated processing as complex nanomaterials. The serum stability of DNA nanotubes and six-helix bundle structures was further examined at different periods after incubation with 10% FBS. DNA nanotubes assembled

with metformin remained intact after 24 h of incubation, while the  $Mg^{2+}$ -assembled nanotubes showed structural decay after 6 h of incubation and had almost disappeared at 24 h (Fig. 3E). A similar phenomenon was also observed for the six-helix bundle structure. Degradation of the  $Mg^{2+}$ -assembled six-helix bundle structure became more pronounced at 24 h, as indicated by the slower movement of the disrupted structure compared to the control band (Fig. 3F). These results indicated that metformin indeed confers new and favorable properties on metformin/DNA nanocomplexes.

#### Cellular uptake and anticancer effects of metformin-assembled KRAS<sup>G12C</sup> siRNA-carrying DNA nanotubes

To validate the potential of the metformin/DNA nanocomplex as a functional nanoplatform for biomedical applications, the abovementioned DNA nanotube structures with six overhangs complementary to the KRAS<sup>G12C</sup> siRNA sequence (NT<sup>MF</sup>K) were used for a proof-of-concept study<sup>25</sup>. DNA nanotubes carrying six KRAS<sup>G12C</sup> siRNAs on each particle were successfully synthesized at high yield (Fig. S6). We first examined the cellular uptake of metformin-assembled DNA nanotubes (NT<sup>MF</sup>) by confocal laser scanning microscopy in two KRAS<sup>G12C</sup>-mutated NSCLC cell lines. Without the assistance of transfection reagents, Cy5-tagged NT<sup>MF</sup> was readily taken up by both H358 and H23 cells, while the same structure assembled in TAE/ $Mg^{2+}$  (NT<sup>Mg</sup>) showed less cellular internalization (Fig. 4A). Fluorescence-activated cell sorting (FACS) further confirmed the increased cellular uptake of NT<sup>MF</sup> compared to NT<sup>Mg</sup> under the same experimental conditions (Fig. 4B). Quantification analysis indicated that 2.74- and 1.49-fold more NT<sup>MF</sup> than NT<sup>Mg</sup> was internalized by H358 and H23 cells, respectively (right panel in Fig. 4B). Note that the metformin concentration was minimized, and KRAS<sup>G12C</sup> siRNA was not conjugated to the structure to avoid influencing cellular uptake in these two experiments. The higher cellular uptake efficiency of NT<sup>MF</sup> might result from surface property differences between NT<sup>MF</sup> and conventionally prepared NT<sup>Mg</sup>. This phenomenon was also observed in spermidine-assembled DNA nanostructures<sup>19</sup> and polylysine-wrapped DNA structures<sup>16</sup>.

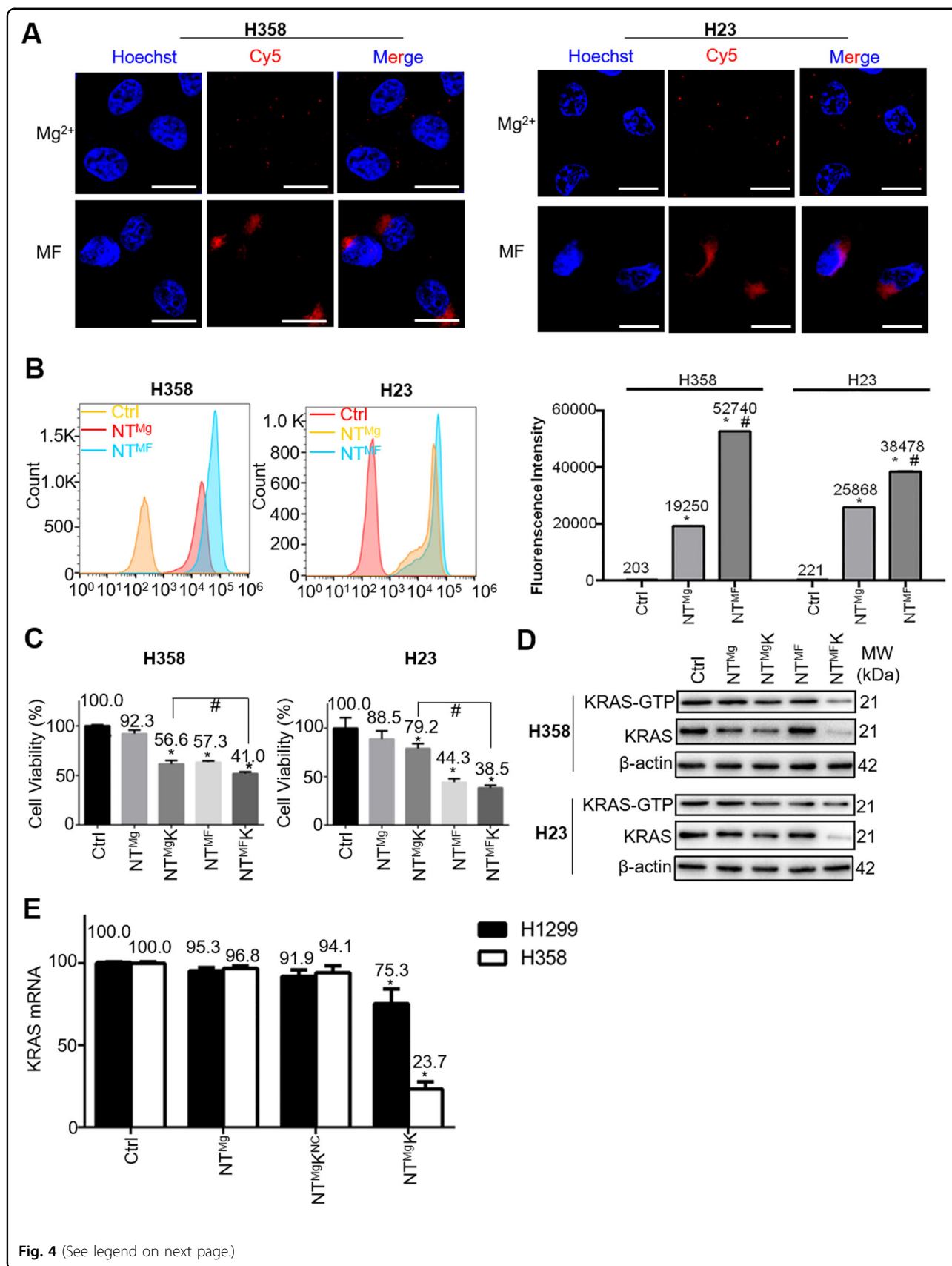
Next, the *in vitro* anticancer effects of NT<sup>MF</sup>K in KRAS<sup>G12C</sup>-mutated NSCLC cells were evaluated by MTT and western blot assays. In the current experimental setting, the G12C-mutated NSCLC cell lines H358 and H23 were selected for *in vitro* study. Accordingly, siRNA that specifically targeted the G12C mutation was employed for KRAS gene knockdown. The target sequences of the wild-type and G12C-mutated KRAS were blasted and are shown in Fig. S7. DNA nanotubes were assembled in TAE/ $Mg^{2+}$  buffer with or without KRAS<sup>G12C</sup> siRNA (NT<sup>Mg</sup>K and NT<sup>Mg</sup>, respectively), and metformin-assembled DNA nanotubes without siRNA

(NT<sup>MF</sup>) were also synthesized and applied as controls. The RT-qPCR results indicated that the knockdown efficiency of the duplex G12C siRNA in H358 cells was up to 77% (Fig. S8). As shown in Fig. 4C, H358 cell growth was strongly inhibited by both NT<sup>MF</sup> and NT<sup>Mg</sup>K, indicating that KRAS<sup>G12C</sup> siRNA and metformin delivered by the DNA nanotubes individually took effect as anticancer drugs. When siRNA and metformin were combined, NT<sup>MF</sup>K-treated cells showed a much lower cell viability of 41.0% compared to NT<sup>MF</sup>- and NT<sup>Mg</sup>K-treated cells. Similarly, the superior tumor cell suppressive effect of NT<sup>MF</sup>K compared to that of NT<sup>MF</sup> and NT<sup>Mg</sup>K was also observed in another KRAS<sup>G12C</sup>-mutated cell line, H23 cells (Fig. 4C, right panel). Western blotting results showed that NT<sup>Mg</sup>K indeed knocked down GTP-bound Ras and KRAS expression and that NT<sup>MF</sup>K knocked down both proteins to an even greater extent in H358 cells (Fig. 4D). As expected, pure DNA nanotubes (NT<sup>Mg</sup>) and metformin/DNA nanotubes without KRAS siRNA (NT<sup>MF</sup>) did not influence their expression. In H23 cells, NT<sup>MF</sup>K also significantly knocked down KRAS GTP levels and KRAS expression (Fig. 4D, lower panel). The results of western blotting in both cell lines correlated well with those of MTT assays for all sample groups and implied a synergistic anticancer effect of NT<sup>MF</sup>K (see Fig. S9 for quantification analysis). In addition, we examined the specificity of G12C siRNA in both G12C-mutated cells (H358 cells) and wild-type cells (H1299 cells). After conjugation with DNA nanotubes, G12C siRNA significantly silenced KRAS mRNA expression in H358 cells. Nevertheless, the knockdown efficiency of NT<sup>Mg</sup>K was greatly weakened in the wild-type NSCLC cell line H1299, as expected (Fig. 4E). The specificity of G12C siRNA on the G12C mutation was also validated by MTT assay. NT<sup>Mg</sup>K had a cell growth inhibitory efficiency of 55.7% on H358 cells compared to 10.5% on wild-type H1299 cells (Fig. S10).

Metformin is a highly potent anticancer drug and may have potential cytotoxicity. We thus examined the cytotoxicity of pure metformin in H358 cells (Fig. S11). Its IC<sub>50</sub> was estimated to be ~40 mM. To eliminate this issue for future applications, polyethylene glycol (PEG, M.W. 8000) was used as an additive during metformin-induced DNA self-assembly. The minimum required metformin concentration for DNA self-assembly was successfully reduced to 50 mM in the presence of 20 mM PEG (Fig. S12). In addition, the cytotoxicity of both NT<sup>MF</sup> and NT<sup>MF</sup>K was dramatically decreased by ~30% in the presence of PEG (Fig. S13).

#### *In vivo* anticancer effects of metformin-assembled KRAS<sup>G12C</sup> siRNA carrying DNA nanotubes

To further test the anticancer performance of NT<sup>MF</sup>K *in vivo*, an H358 cell-implanted immunodeficient mouse model was applied in the current study. DNA nanotubes



(see figure on previous page)

**Fig. 4 Cellular uptake and anticancer effects of metformin-assembled DNA nanotube in vitro.** **A** Evaluation of DNA nanotube cellular uptake in vitro. Confocal laser scanning microscopy (CLSM) imaging of H358 (left) and H23 (right) cells treated with DNA nanotubes. DNA nanotubes loaded with fluorescent Cy5 were incubated with cells for 12 h before imaging. The Cy5 concentration was maintained at 300 nM. Scale bar: 20  $\mu$ m. **B** Flow cytometry analysis of DNA nanotubes internalized by H358 and H23 cells. The right panel shows the quantification analysis of the internalization efficiencies. Cells were administered metformin at a concentration of 5 mM in both experiments. **C** MTT assay showed in vitro anticancer cell proliferation effects on different drug formulations. NT<sup>MF</sup>K-treated groups exhibited enhanced killing effects compared with KRAS<sup>G12C</sup> siRNA or metformin alone in both H358 and H23 cells. **D** Western blotting showed KRAS-GTP levels and KRAS protein expression in H358 and H23 cells. **E** RT-qPCR results indicated that G12C siRNA specifically reduced KRAS mRNA levels in G12C-mutated H358 cells but had a much lower effect on wild-type H1299 cells. The data are representative of five separate experiments (mean  $\pm$  S.E.,  $n = 5$ ). Statistical analysis: one-way ANOVA and Tukey's multiple comparison test,  $P$  values: \* $P < 0.05$  vs. Ctrl, # $P < 0.05$ . # indicates connected pairs.

tagged with Cy5.5 were injected into mouse tail veins and examined at different time points. The biodistribution of DNA nanotubes in mice was then imaged with a Vilber Lourmat imaging system. DNA nanotubes effectively accumulated in tumor sites after 1 h (Fig. 5A). After 9 h, the fluorescence intensity remained very high. Other organs (the liver and kidneys) also exhibited substantial nanoparticle accumulation, as shown in Fig. 5B. The current metformin/DNA complex nanoplateform is not conjugated to any targeting moiety; thus, the passive delivery of DNA nanomaterials into tumor sites is due mainly to the enhanced permeability and retention (EPR) effect. We then evaluated the anticancer capability of NT<sup>MF</sup>K in mice. Other nanomaterial groups, NT<sup>Mg</sup>, NT<sup>Mg</sup>K, and NT<sup>MF</sup>, were also tested as controls. All nanomaterials or saline was injected into the mice three times on alternating days. Tumor size was recorded every 3 days to evaluate the anticancer effect of the nanomaterials. The tumors in both NT<sup>Mg</sup>K- and NT<sup>MF</sup>-treated mice were much smaller than those in saline- and pure DNA-treated mice. The tumor growth of NT<sup>MF</sup>K-treated mice was greatly suppressed compared to that of the saline and NT<sup>Mg</sup> groups (Fig. 5C). The tumors were then retrieved and measured for comparison (Fig. 5D). The mouse weights for all sample groups remained roughly the same during the study (Fig. 5E). The RT-qPCR results showed that the KRAS mRNA levels in NT<sup>MF</sup>K-treated mouse tumors, lungs, and kidneys were 30%, 99%, and 86%, respectively, which implied a low side effect on major organs (Fig. S14). These results are in accordance with the results of in vitro MTT assays and suggest that NT<sup>MF</sup>K indeed has a more potent antitumor effect than KRAS<sup>G12C</sup> siRNA or metformin therapy alone. Further histological and immunohistochemistry (IHC) analyses were performed (Fig. 5F). Tumor tissues from NT<sup>Mg</sup>K-, NT<sup>MF</sup>-, and NT<sup>MF</sup>K-treated mice were subjected to hematoxylin and eosin (H&E) staining and displayed apparent nuclear shrinkage and vacuolization, indicating strong damage to the tumors. KRAS expression was notably decreased in NT<sup>Mg</sup>K- and NT<sup>MF</sup>K-treated tissues, as shown in the middle panel of Fig. 5F. As expected, Ki67 staining was markedly reduced in NT<sup>MF</sup>K-treated

tumors. These data suggested that both metformin and siRNA independently exert moderate anticancer effects. More importantly, NT<sup>MF</sup>K comprising metformin and siRNA had a stronger therapeutic effect in vivo than metformin or siRNA alone.

#### Mechanism of the synergistic anticancer effects

To elucidate the underlying mechanism by which NT<sup>MF</sup>K combats KRAS<sup>G12C</sup>-mutated NSCLC cancer, western blotting was employed to identify the signaling pathways involved. As demonstrated by the aforementioned results, NT<sup>MF</sup>K had a much more pronounced therapeutic effect than NT<sup>Mg</sup>K and NT<sup>MF</sup>, which strongly implies that metformin and siRNA exert synergistic effects. Metformin activates adenosine monophosphate-activated protein kinase (AMPK) and subsequently downregulates phosphorylated mammalian target of rapamycin (mTOR), which links metformin to cell growth and proliferation<sup>26</sup>. In our system, when the effects of metformin and siRNA were assessed separately, NT<sup>MF</sup> (metformin)-treated cells exhibited elevated phosphorylated AMPK levels and decreased phosphorylated mTOR levels (Fig. 6A). For KRAS, NT<sup>Mg</sup>K treatment knocked down KRAS expression, decreased phosphorylated AKT levels, and subsequently decreased phosphorylated mTOR (p-mTOR) levels. While both metformin and KRAS<sup>G12C</sup> siRNA downregulated p-mTOR, they inhibited cancer cell growth more effectively when applied together. As hypothesized, NT<sup>MF</sup>K substantially decreased p-mTOR due to overlap between the two signaling pathways that were activated by KRAS G12C siRNA and metformin. A similar trend was also observed in another G12C-mutated cell line, H23 cells (Fig. 6B). Taken together, these results demonstrated that the synergistic anticancer effects of NT<sup>MF</sup>K are attributed to the dual targeting of mTOR from the AMPK-mTOR pathway (downstream of metformin) and the KRAS-AKT-mTOR pathway (see quantification analysis of western blotting in Fig. S15).

#### Discussion

KRAS is a critical gene controlling cell growth, maturation, and death through the downstream RAF-

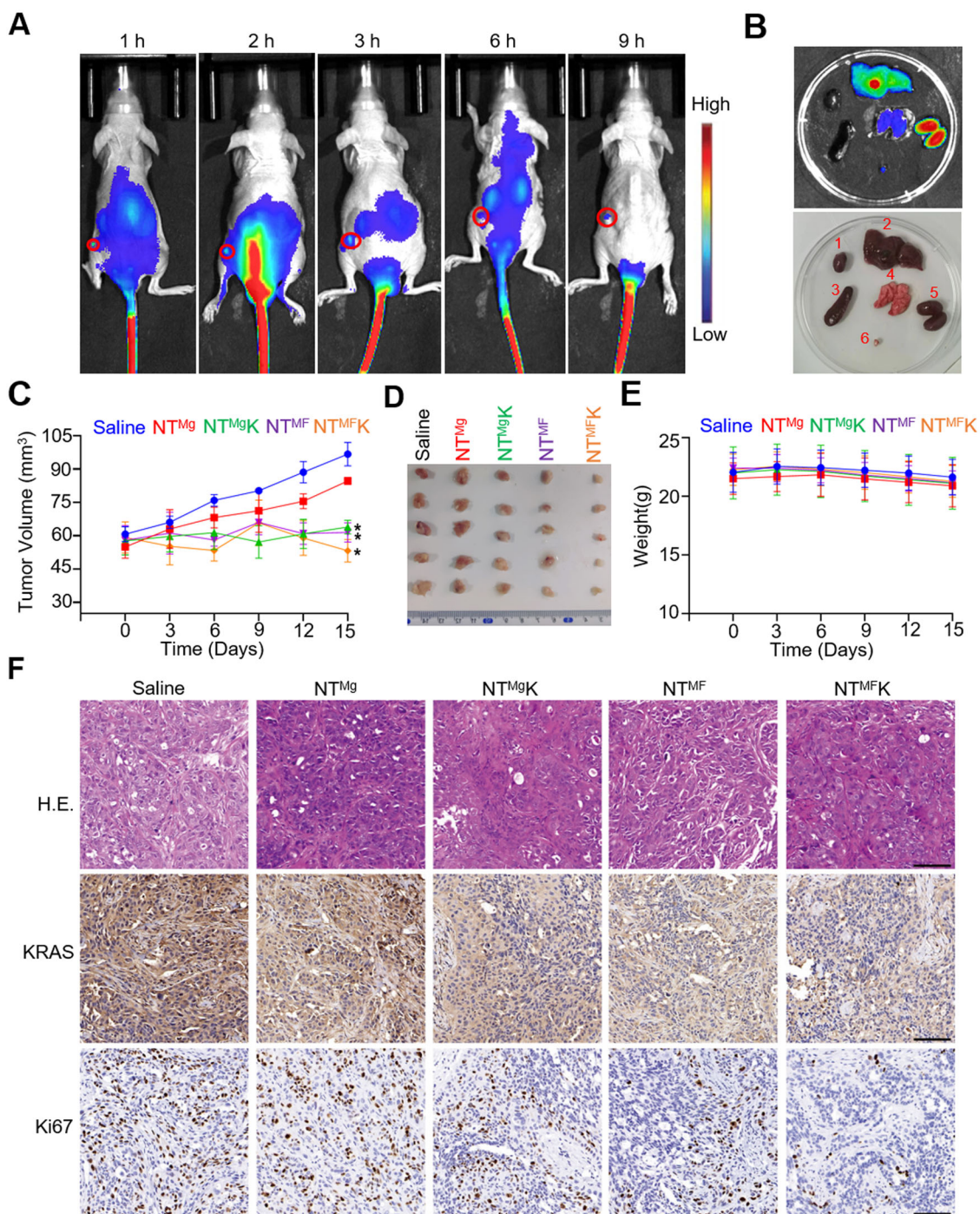


**Fig. 5** Biodistributions and anticancer therapeutic effects of metformin/DNA nanocomplexes in vivo. **A** Biodistributions of DNA nanotubes in mice at different periods after tail injection. **B** Images showing fluorescent DNA nanotubes in different major organs after 9 h. 1. Heart, 2. Liver, 3. Spleen, 4. Lung, 5. Kidney, 6. Tumor. **C** Changes in tumor volume in different sample groups during treatment. Arrows indicate the administration time points. **D** Tumors were dissected from mice after 15 days. **E** Statistical analysis of mouse weights for all groups during the treatment. **F** H&E staining, IHC staining for KRAS, and Ki67 staining. Scale bar: 50  $\mu$ m. The data are representative of six separate experiments (mean  $\pm$  S.E.,  $n = 6$ ). Statistical analysis: one-way ANOVA and Tukey's multiple comparison test,  $P$  values: \* $P < 0.05$  vs. saline group.

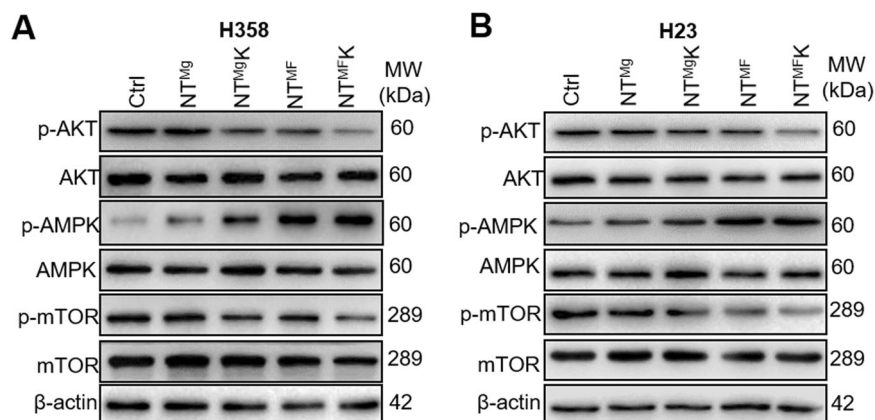


**Fig. 6** The underlying mechanism of the synergistic anticancer effects of metformin/DNA nanocomplexes. **A** Effects of different nanomaterial treatments on AKT/AMPK-mTOR pathways in H358 cells. **B** Effects of different nanomaterial treatments on AKT/AMPK-mTOR pathways in H23 cells. Analyses were performed as in Fig. 5F. Tumor tissues from  $NT^{MgK}$ -,  $NT^{MF}$ -, and  $NT^{MFK}$ -treated mice were subjected to hematoxylin and eosin (H&E) staining and displayed visible nuclear shrinkage and vacuolization, indicating strong damage to the tumors. KRAS expression was notably decreased in  $NT^{MgK}$ - and  $NT^{MFK}$ -treated tissues, as shown in the middle panel of Fig. 5F. As expected, Ki67 staining was markedly reduced in  $NT^{MFK}$ -treated tumors. These data suggested that both metformin and siRNA independently exert moderate anticancer effects. More importantly,  $NT^{MFK}$  comprising metformin and siRNA had a stronger therapeutic effect in vivo than metformin or siRNA alone.

MEK<sub>1/2</sub>-ERK<sub>1/2</sub> and PI3K-AKT signaling pathways. Numerous reports have demonstrated that frequent mutations in the KRAS gene have been detected in human cancers, including non-small cell lung cancer (NSCLC) and pancreatic cancer. KRAS mutation drives tumorigenesis and tumor maintenance by the continuous activation and accumulation of GTP-bound Ras, which triggers downstream oncogenic signaling pathways. Unfortunately, there is no effective inhibitor to block mutant KRAS protein directly due to the lack of hydrophobic pockets for small molecule binding. Strategies aimed at targeting MEK, which is downstream of KRAS, using selumetinib or trametinib in phase II clinical trials failed<sup>27–29</sup>. Gene therapy is a promising strategy to combat cancer. The first FDA-approved siRNA drug, Onpatro, sheds light on small nucleic acid drugs and is an excellent option for cancer treatment. The complexity of KRAS mutations is that they have multiple point mutations, and the allelic genotypes make a large difference when using RNA interference technology. It was reported that wild-type KRAS acts as a tumor suppressor in KRAS mutant cancer cells<sup>30,31</sup>. KRAS gene knockdown without distinguishing mutation types (such as G12C, G12V, G12D, or G12S) may inhibit wild-type KRAS expression and potentially normal cell growth. The combination of siRNA and the anticancer drug metformin achieved excellent antitumor performances in the current study. In addition to the synergistic effects of metformin and KRAS<sup>G12C</sup> siRNA on the mTOR pathway (Fig. S16), Ma et al. reported that mutant KRAS is more sensitive than wild-type KRAS to metformin-mediated apoptosis induction and proliferation inhibition. The selective

targeting of mutant KRAS by metformin may decrease the off-target effects of  $NT^{MFK}$ <sup>32</sup>.

In addition, the current study demonstrated that metformin organized component DNA strands into well-defined nanostructures in aqueous systems without other components. The positive charge of guanidine groups, similar to other cationic molecules, in aqueous solution appears to be responsible for successful DNA assembly<sup>19</sup>. The formation of these four DNA structures also demonstrated that metformin can organize defined DNA nanostructures regardless of the design strategy (tile-based or origami) and structure complexity. The stability of metformin/DNA nanostructures as a whole and their integrity in physiological settings are critical factors for the potential biomedical application of this novel nanoplatform. The higher serum stability of metformin-assembled DNA nanocomplexes compared to  $Mg^{2+}$ -assembled DNA nanocomplexes might be due to the shielding effect of the molecular structure of metformin but requires further investigation.

In summary, we have demonstrated that guanidine group-containing molecules, particularly the anticancer drug metformin, can mediate DNA self-assembly into defined tile-based and origami nanostructures. The obtained metformin/DNA complex nanomaterials were shown to be stable in physiological settings and showed better biocompatibility than conventional  $Mg^{2+}$ -assembled DNA nanostructures. This finding is probably due to the strong binding between the guanidine group and DNA and the shielding effect of metformin in the nanocomplex. Further in vitro and in vivo studies indicated that a metformin/DNA nanoplatform carrying metformin

and KRAS G12C-specific siRNA showed excellent anticancer properties. The excellent therapeutic efficacy of this nanoplatform is attributed to the synergistic effects of siRNA and metformin, which both inhibited mTOR and consequently cancer cell proliferation. The results of the current study suggest that assembling defined DNA nanostructures with functional molecules, such as metformin, is a promising way to confer new functionalities to DNA nanostructures. Such new complex nanomaterials hold great potential for future applications in multiple research fields.

#### Acknowledgements

We thank Prof. Pengfei Wang from Shanghai Jiao Tong University for his support with DNA origami design and Prof. Qiaonan Guo and Dr. Yangfan Lv from the Pathology Department of Xinqiao Hospital for their technical support with IHC experiments. We thank the College of Pharmaceutical Sciences, Southwest University for technical assistance in AFM imaging (Bruker Multimode 8). This work was supported by the National Natural Science Foundation of China (32071379, 81670047, 82070071) and the National Natural Science Foundation of Chongqing, China (cstc2021ycjh-bgzxm0011).

#### Author details

<sup>1</sup>Institute of Respiratory Diseases, Xinqiao Hospital, Third Military Medical University, Chongqing 400037, China. <sup>2</sup>Department of Respiratory Medicine, Jinling Hospital, Nanjing University, Nanjing, China. <sup>3</sup>Department of Pulmonary and Critical Care Medicine, Zhongshan Hospital, Fudan University, Shanghai, China. <sup>4</sup>Laboratory of Pharmacy and Chemistry, and Laboratory of Tissue and Cell Biology, Lab Teaching & Management Center, Chongqing Medical University, Chongqing, China. <sup>5</sup>Department of Chemical and Biomolecular Engineering, National University of Singapore, Singapore, Singapore

#### Author contributions

Conceptualization: H.Q., D.L., and G.W.; methodology: H.Q., B.H., and Q.L.; investigation: H.Q., D.W., B.H., Y.X., D.W., C.C., and W.Z.; writing—original draft: H.Q., Q.L., and Y.X.; writing—review & editing: H.Q., D.L., and G.W.; supervision: D.L. and G.W.; funding acquisition: H.Q. and G.W.

#### Competing interests

The authors declare no competing interests.

#### Ethics statement

Full experimental procedures are provided in the Supplemental Information. All animal experimental procedures were performed in compliance with the Laboratory Animal Welfare and Ethics Committee of Third Military Medical University. The accreditation number is TY20170075, 20165128.

#### Publisher's note

Springer Nature remains neutral with regard to jurisdictional claims in published maps and institutional affiliations.

**Supplementary information** The online version contains supplementary material available at <https://doi.org/10.1038/s41427-022-00427-y>.

Received: 12 November 2021 Revised: 8 August 2022 Accepted: 11 August 2022.

Published online: 7 October 2022

#### References

- Li, S. et al. A DNA nanorobot functions as a cancer therapeutic in response to a molecular trigger. *Nat. Biotechnol.* **36**, 258 (2018).
- Mou, Q. et al. DNA Trojan horses: self-assembled floxuridine-containing DNA polyhedra for cancer therapy. *Chem. Int. Ed.* **56**, 12528–12532 (2017).
- Guo, Y. Y. et al. Stressing the role of DNA as a drug carrier: synthesis of DNA-drug conjugates through grafting chemotherapeutics onto phosphorothioate oligonucleotides. *Adv. Mater.* **31**, e1807533 (2019).
- Zhao, Y. X., Zeng, A. S. X., Benson, E., Nyström, A. M. & Högberg, B. DNA origami delivery system for cancer therapy with tunable release properties. *ACS Nano* **6**, 8684–8691 (2012).
- Lee, H. et al. Molecularly self-assembled nucleic acid nanoparticles for targeted in vivo siRNA delivery. *Nat. Nanotechnol.* **7**, 389–393 (2012).
- Jiang, Q. et al. DNA origami as a carrier for circumvention of drug resistance. *J. Am. Chem. Soc.* **134**, 13396–13403 (2012).
- Pei, H. et al. DNA nanostructure-based biomolecular probe carrier platform for electrochemical biosensing. *Adv. Mater.* **22**, 4754–4758 (2010).
- Tay, C. Y., Yuan, L. & Leong, D. T. Nature-inspired DNA nanosensor for real-time in situ detection of mRNA in living cells. *ACS Nano* **9**, 5609–5617 (2015).
- Modi, S. et al. A DNA nanomachine that maps spatial and temporal pH changes inside living cells. *Nat. Nanotechnol.* **4**, 325–330 (2009).
- Giovanni, M. et al. Biosensors: electrochemical quantification of *Escherichia coli* with DNA nanostructure. *Adv. Funct. Mater.* **25**, 3979 (2015).
- Jungmann, R. et al. Multiplexed 3D cellular super-resolution imaging with DNA-PAINT and exchange-PAINT. *Nat. Methods* **11**, 313–318 (2014).
- Bhatia, D., Surana, S., Chakraborty, S., Koushika, S. P. & Krishnan, Y. A synthetic icosahedral DNA-based host-cargo complex for functional in vivo imaging. *Nat. Commun.* **2**, 339 (2011).
- Hu, Q., Li, H., Wang, L., Gu, H. & Fan, C. DNA nanotechnology-enabled drug delivery systems. *Chem. Rev.* **119**, 6459–6506 (2019).
- Jiang, Q. et al. Rationally designed DNA-based nanocarriers. *Adv. Drug. Deliv. Rev.* **147**, 2–21 (2019).
- Nielsen, T. B. et al. Peptide-directed DNA-templated protein labelling for the assembly of a pseudo-igM. *Angew. Chem. Int. Ed. Engl.* **58**, 9068–9072 (2019).
- Ponnuswamy, N. et al. Oligolysine-based coating protects DNA nanostructures from low-salt denaturation and nuclease degradation. *Nat. Commun.* **8**, 15654 (2017).
- Auvinen, H. et al. Protein coating of DNA nanostructures for enhanced stability and immunocompatibility. *Adv. Healthc.* **6**, 1700692 (2017).
- Chopra, A., Krishnan, S. & Simmel, F. C. Electrotransfection of polyamine folded DNA origami structures. *Nano Lett.* **16**, 6683–6690 (2016).
- Wang, D. et al. Isothermal self-assembly of spermidine-DNA nanostructure complex as a functional platform for cancer therapy. *ACS Appl. Mater. Interfaces* **10**, 15504–15516 (2018).
- Zhao, Y. et al. PolyMetformin combines carrier and anticancer activities for in vivo siRNA delivery. *Nat. Commun.* **7**, 11822 (2016).
- Zhang, T., Tian, T. & Lin, Y. F. Functionalizing framework nucleic-acid-based nanostructures for biomedical application. *Adv. Mater.* e2107820 (2021).
- Tian, T. et al. A Framework nucleic acid based robotic nanobee for active targeting therapy. *Adv. Funct. Mater.* **31**, 2007342 (2020).
- Ma, W. et al. An intelligent DNA nanorobot with in vitro enhanced protein lysosomal degradation of HER2. *Nano Lett.* **19**, 4505–4517 (2019).
- Qian, H. et al. Self-assembly of DNA nanotubes with defined diameters and lengths. *Small* **10**, 855–858 (2014).
- You, Z. et al. Regulation of vascular smooth muscle cell autophagy by DNA nanotube-conjugated mTOR siRNA. *Biomaterials* **67**, 137–150 (2015).
- Han, G., Gong, H., Wang, Y., Guo, S. & Liu, K. AMPK/mTOR-mediated inhibition of survivin partly contributes to metformin-induced apoptosis in human gastric cancer cell. *Cancer Biol.* **16**, 77–87 (2015).
- Jänne, P. A. et al. Selumetinib plus docetaxel compared with docetaxel alone and progression-free survival in patients with KRAS-mutant advanced non-small cell lung cancer: the SELECT-1 randomized clinical trial. *JAMA* **317**, 1844–1853 (2017).
- Blumenschein, G. R. J. et al. A randomized phase II study of the MEK1/MEK2 inhibitor trametinib (GSK1120212) compared with docetaxel in KRAS-mutant advanced non-small-cell lung cancer (NSCLC). *Ann. Oncol.* **26**, 894–901 (2015).
- Wang, J., Yao, X. & Huang, J. New tricks for human farnesyltransferase inhibitor: cancer and beyond. *Medchemcomm* **8**, 841–854 (2017).
- Ambrogio, C. et al. KRAS dimerization impacts MEK inhibitor sensitivity and oncogenic activity of mutant KRAS. *Cell* **172**, 857–868 (2018).
- Singh, A., Sowjanya, A. P. & Ramakrishna, G. The wild-type Ras: road ahead. *FASEB J.* **19**, 161–169 (2005).
- Ma, Y. et al. K-ras gene mutation as a predictor of cancer cell responsiveness to metformin. *Mol. Med. Rep.* **8**, 763–768 (2013).